# **INORGANIC** CHEMISTRY







**FRONTIERS** 

#### RESEARCH ARTICLE

View Article Online
View Journal | View Issue



**Cite this:** *Inorg. Chem. Front.*, 2023, **10**, 2708

# Atomically isolated and unsaturated Sb sites created on $Sb_2S_3$ for highly selective NO electroreduction to $NH_3\dagger$

Kai Chen, Ying Zhang, Wenyu Du, Yali Guo and Ke Chu 10 \*

Sb<sub>2</sub>S<sub>3</sub> comprising an atomically isolated and unsaturated Sb (Sb<sub>AIU</sub>) site is demonstrated as a fascinating catalyst for highly selective electrochemical NO-to-NH<sub>3</sub> conversion (NORR). Theoretical calculations reveal the crucial function of Sb<sub>AIU</sub> sites to favor the adsorption and activation of NO, accelerate the protonation energetics of the NO-to-NH<sub>3</sub> pathway and impede the coverage of H<sub>2</sub>O/H species, thereby boosting both NORR activity and selectivity. Consequently, the developed Sb<sub>AIU</sub>-rich Sb<sub>2</sub>S<sub>3</sub> catalyst exhibits an excellent NO-to-NH<sub>3</sub> faradaic efficiency of 93.7% and a high NH<sub>3</sub> yield rate of 168.6  $\mu$ mol h<sup>-1</sup> cm<sup>-2</sup>, representing the highest NORR selectivity among all reported NORR catalysts.

Received 14th February 2023, Accepted 28th March 2023 DOI: 10.1039/d3qi00268c

rsc.li/frontiers-inorganic

#### 1. Introduction

Ammonia is a pivotal chemical that is widely applied in many aspects of social and economic development. Recently,  $N_2$  electrofixation emerged as a promising technology for green  $NH_3$  synthesis, whereas its efficiency is greatly limited by intractable issues of ultrastable  $N\equiv N$  bonds. Alternatively, NO possesses a relatively low  $N\equiv O$  bond energy and thus electrochemical NO-to- $NH_3$  conversion (NORR) represents a more prospective approach than  $N_2$  electrofixation for  $NH_3$  electrosynthesis. Nevertheless, the NORR effectiveness is greatly retarded by the sophisticated five-electron reaction process and severe competition from the hydrogen evolution reaction (HER), and it is imperative to explore efficient NORR electrocatalysts capable of boosting the NO-to- $NH_3$  pathway with high selectivity.

Transition metal-based catalysts commonly exhibit high NORR activity owing to their partially occupied d-orbitals boosting NO adsorption. Nevertheless, d-orbitals also favor the formation of metal—H bonds to trigger the competitive HER, giving rise to low NORR selectivity. Promisingly, main group p-block metals (Sb, In, Bi, *etc.*) are catalytically inert in the HER because of their closed d-band shells. Meanwhile, the partially occupied p-orbitals in p-block metals are confirmed to be active for N—O bond dissociation, making p-block metal-based materials promising as a new class of NORR catalysts. P-block Sb-based catalysts are appealing

School of Materials Science and Engineering, Lanzhou Jiaotong University, Lanzhou 730070, China. E-mail: chuk630@mail.lzitu.cn

†Electronic supplementary information (ESI) available. See DOI: https://doi.org/ 10.1039/d3qi00268c NORR candidates owing to the great capability of Sb sites to impede the HER and activate the nitrogen-containing molecules.<sup>35</sup> On the other hand, catalysts with atomically isolated sites are known to present outstanding catalytic performance because of their high atom utilization and optimal binding with intermediates and reactants.<sup>36–38</sup> Besides, defect engineering by creating vacancies or unsaturated sites is considered an effective strategy to tailor the electronic structure of catalysts with enhanced catalytic activities.<sup>39–41</sup> In view of the above, creating atomically isolated and unsaturated Sb sites is therefore an attractive strategy for designing high-efficiency NORR catalysts.

In this study, p-block  $Sb_2S_3$  is designed as a fascinating catalyst for highly selective NORR, which exhibits an excellent NO-to-NH $_3$  faradaic efficiency ( $FE_{NH}_3$ ) of 93.7% and a high NH $_3$  yield rate of 168.6 µmol h $^{-1}$  cm $^{-2}$ , representing the highest NORR selectivity among all reported NORR catalysts. Detailed structural characterization and theoretical computations reveal that atomically isolated and unsaturated Sb sites created on  $Sb_2S_3$  play a crucial role in greatly enhancing the NORR activity and selectivity.

#### 2. Results and discussion

A solvothermal method was utilized to synthesize  $Sb_2S_3$ . The XRD pattern of the as-synthesized  $Sb_2S_3$  (Fig. 1a) shows distinct peaks that are assigned to the pure orthorhombic  $Sb_2S_3$  phase with a good crystallinity. The SEM image of  $Sb_2S_3$  (Fig. 1b) shows a typical nanoflower morphology consisting of numerous vertically aligned nanosheets. The nanosheet feature can be further confirmed by the TEM image (Fig. 1c).

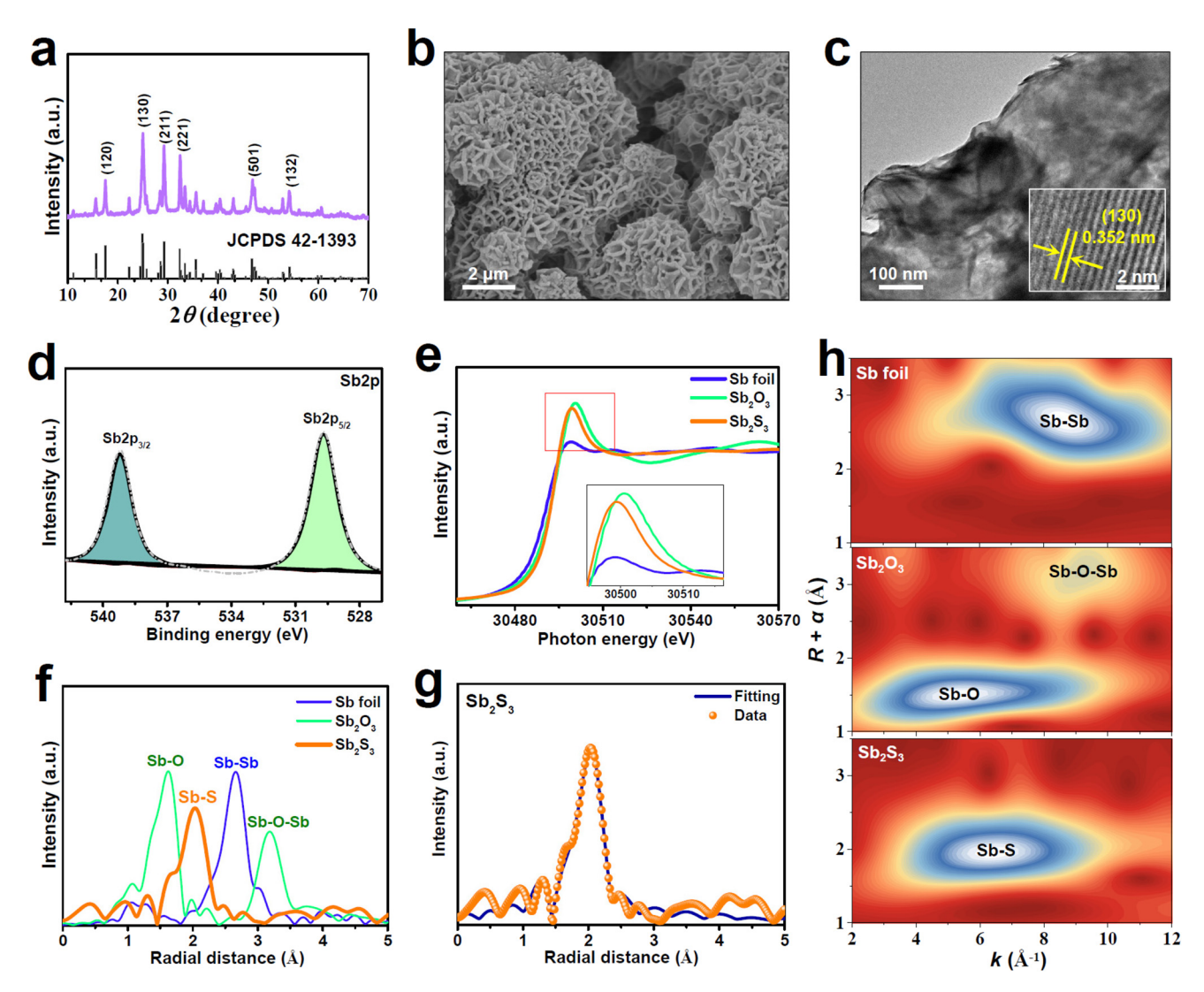


Fig. 1 Characterization of Sb<sub>2</sub>S<sub>7</sub>: (a) XRD pattern, (b) SEM image, (c) TEM image and HRTEM image (inset), (d) XPS Sb2p spectrum, (e) Sb K-edge XANES spectra, (f) EXAFS spectra and (h) WT profiles of Sb<sub>2</sub>S<sub>3</sub> and reference samples. (g) EXAFS fitting curve of Sb<sub>2</sub>S<sub>3</sub>.

As shown in the HRTEM image (Fig. 1c, inset), the lattice spacing of Sb<sub>2</sub>S<sub>3</sub> nanosheets is determined to be 0.352 nm, corresponding to the (130) facet of orthorhombic Sb<sub>2</sub>S<sub>3</sub>, in line with the XRD result (Fig. 1a). The XPS Sb spectrum of Sb<sub>2</sub>S<sub>3</sub> (Fig. 1d) can be split into  $Sb^{3+}2p_{3/2}$  (539.3 eV) and  $Sb^{3+}2p_{5/2}$ (529.8 eV), while the deconvolution of the S2p spectrum (Fig. S1†) shows two peaks of  $S2p_{1/2}$  (163.6 eV) and  $S2p_{3/2}$ (161.8 eV), in good accordance with those reported for Sb<sub>2</sub>S<sub>3</sub>.42-44

We employ X-ray absorption near-edge structure (XANES) and extended X-ray absorption fine structure (EXAFS) characterizations to further examine the valence states and coordination structures of Sb<sub>2</sub>S<sub>3</sub>. The Sb K-edge XANES spectra (Fig. 1e) show that the white line of Sb<sub>2</sub>S<sub>3</sub> is slightly lower than that of Sb<sub>2</sub>O<sub>3</sub>, suggesting the valence state of Sb to be smaller than the intrinsic Sb valence of Sb<sub>2</sub>S<sub>3</sub> (+3), which is caused by the presence of coordinatively unsaturated Sb sites in Sb<sub>2</sub>S<sub>3</sub>.

The Sb K-edge EXAFS spectra (Fig. 1f) show that Sb<sub>2</sub>S<sub>3</sub> exhibits a dominant peak at 2.03 Å assignable to the Sb-S bond, which largely differs from those of Sb foil (Sb-Sb: 2.66 Å) and Sb<sub>2</sub>O<sub>3</sub> (Sb-O: 1.62 Å, Sb-O-Sb: 3.18 Å), indicating that  $Sb_2S_3$  comprises the isolated state of Sb and no oxidized Sb species are present on Sb<sub>2</sub>S<sub>3</sub>. Likewise, the corresponding wavelet transform (WT) contour plots (Fig. 1h) show only one intensity maximum at 6.3  $\text{Å}^{-1}$  corresponding to the Sb-S coordination, suggesting the existence of atomically dispersed Sb atoms. The EXAFS fitting data (Fig. 1g and Table S1†) reveal the average coordination number (CN) of Sb<sub>2</sub>S<sub>3</sub> to be 4.2, much smaller than the crystallographic value of Sb<sub>2</sub>S<sub>3</sub> (CN = 5), <sup>45</sup> corroborating the existence of plentiful unsaturated Sb sites in Sb<sub>2</sub>S<sub>3</sub>. These XAS results reveal that the prepared Sb<sub>2</sub>S<sub>3</sub> naturally contains abundant atomically isolated and unsaturated Sb (Sb<sub>AIII</sub>) sites, which are considered to be catalytically active towards NORR.

Electrocatalytic NORR measurements were carried out using a gas-tight H-type electrolytic cell containing 0.5 M  $\mathrm{Na_2SO_4}$  solution. Several colorimetric approaches (Fig. S2 and S3†) were performed to detect the liquid products, while the gaseous products were detected by gas chromatography. We conducted linear sweep voltammetry (LSV) measurement to initially assess the NORR activity of  $\mathrm{Sb_2S_3}$ . It is displayed in

Research Article

Fig. 2a that  $Sb_2S_3$  presents a noticeable current density (j) enhancement in the NO-saturated electrolyte relative to the Arsaturated one, proving that  $Sb_2S_3$  has a high NORR activity. We then quantitatively determined the NORR performance of  $Sb_2S_3$  with the integration of chronoamperometry (Fig. 2b) and colorimetric tests at various potentials. As shown in Fig. 2c, with increasing the potential, both the  $NH_3$  yield rate and

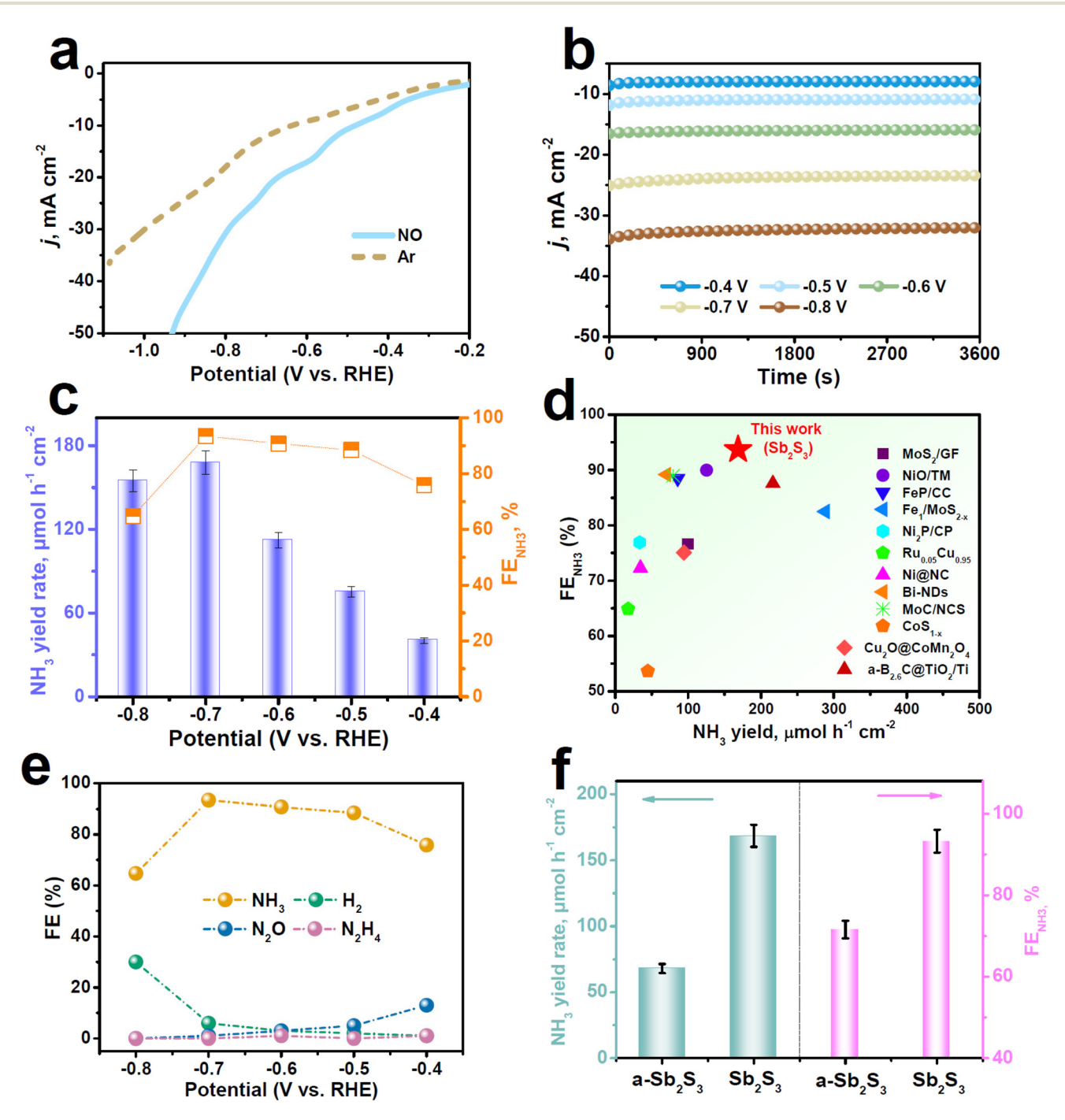


Fig. 2 (a) LSV curves of  $Sb_2S_3$  in Ar/NO-saturated 0.5 M  $Na_2SO_4$ . (b) Chronoamperometry test of  $Sb_2S_3$  at various potentials, and the resulting (c)  $NH_3$  yield rates and  $FE_{NH_3}$ . (d) Comparison of  $NH_3$  yield rates and  $FE_{NH_3}$  between  $Sb_2S_3$  and the recently reported NORR catalysts. (e) FEs of different products on  $Sb_2S_3$  after NORR electrolysis at various potentials. (f)  $NH_3$  yield rates and  $FE_{NH_3}$  of  $Sb_2S_3$  and  $a-Sb_2S_3$  at a-0.7 V.

FE<sub>NH</sub>, of Sb<sub>2</sub>S<sub>3</sub> exhibit a volcanic shape and reach their highest values of 168.6  $\mu$ mol h<sup>-1</sup> cm<sup>-2</sup> and 93.7% at -0.7 V, respectively. Strikingly, as shown in Fig. 2d (see Table S2 for details†), the FE<sub>NH</sub>, of Sb<sub>2</sub>S<sub>3</sub> shows the highest NORR selectivity among all the reported NORR catalysts, while its NH3 yield rate is also superior to those of most reported NORR catalysts. Meanwhile, Fig. 2e shows that the FEs of N-containing side products (N2O and N<sub>2</sub>H<sub>4</sub>) are rather low at all considered potentials, in good accordance with the partial current density data (Fig. S4†), signifying the outstanding NO-to-NH3 selectivity of Sb2S3. Regarding the NORR stability, the chronopotentiometric test presents a stable current density for at least 20 h of electrolysis

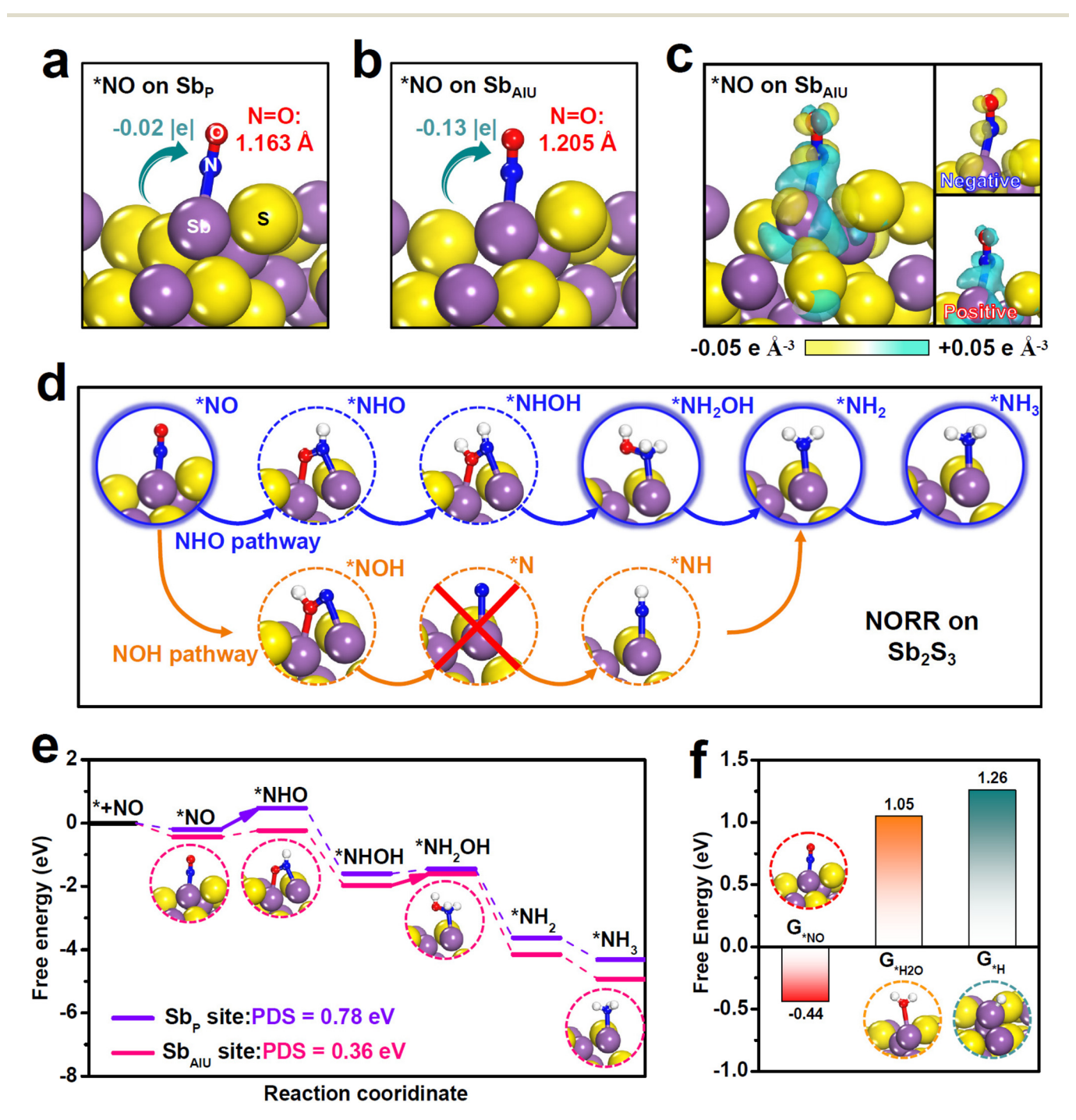


Fig. 3 (a and b) Atomic structures of absorbed NO on (a) the  $Sb_P$  site and (b) the  $Sb_{AIU}$  site of  $Sb_2S_3$ . (c) Charge density difference of \*NO on the Sb<sub>AIU</sub> site (yellow: accumulation; cyan: depletion). (d) Schematic of two NORR pathways (NHO and NOH) on Sb<sub>2</sub>S<sub>3</sub>. (e) Free energy profiles of the NORR process (NHO pathway) on Sb<sub>P</sub> and Sb<sub>AIU</sub>. (f) Binding free energies of \*H<sub>2</sub>O, \*H and \*NO on Sb<sub>AIU</sub>.

(Fig. S5†), and the resulting FE<sub>NH</sub>, shows very small attenuations, indicating the good long-term stability of Sb<sub>2</sub>S<sub>3</sub>. Besides, no remarkable fluctuations in the NH3 yield rate and FE<sub>NH</sub>, occur during the seven electrolysis cycles (Fig. S6†), proving the favorable cycling stability of Sb<sub>2</sub>S<sub>3</sub>.<sup>47-50</sup>

Research Article

We conducted several experiments to verify the NH<sub>3</sub> origin. First, NH<sub>3</sub> is almost undetectable in the control colorimetric tests (Fig. S7†).32 In addition, upon feeding 15NO gas, the resulting <sup>1</sup>H nuclear magnetic resonance (NMR, Fig. S8†) spectra reveal the characteristic 15NH<sub>4</sub> doublets, whereas feeding Ar gas leads to the absence of <sup>15</sup>NH<sub>4</sub><sup>+</sup> doublets. <sup>51–53</sup> Furthermore, the switching NO-Ar test (Fig. S9†) reveals significant NH3 production in NO cycles, whereas NH3 is nearly undetectable in Ar cycles. All these results validate that the produced NH3 stems from the electrochemical NORR process catalyzed by Sb<sub>2</sub>S<sub>3</sub>.

For comparison, we evaluated the NORR property of annealed Sb<sub>2</sub>S<sub>3</sub> (a-Sb<sub>2</sub>S<sub>3</sub>) with much reduced Sb<sub>AIU</sub> (Fig. S10 and Table S1†) under identical measurement conditions at −0.7 V. Impressively, Fig. 2f shows that the NORR performance of a-Sb<sub>2</sub>S<sub>3</sub> is significantly poorer than that of the original Sb<sub>2</sub>S<sub>3</sub>, revealing that the Sb<sub>AIU</sub> sites play a vital role in dramatically boosting the NORR property of Sb<sub>2</sub>S<sub>3</sub>. Electrochemical surface area (ECSA, Fig. S11 and S12†) measurements show that the ECSA-normalized NORR performances of the two catalysts (Fig. S13†) present the same trend as that shown in

Fig. 2f. Besides, both catalysts have comparable charge transport kinetics (Fig. S14†).54-57 These findings demonstrate the intrinsic superior NORR property of Sb<sub>2</sub>S<sub>3</sub>.

Theoretical computations were carried out to shed light on the boosted NORR property of Sb<sub>2</sub>S<sub>3</sub>. To start, we evaluated the adsorption behaviors of the NO molecule on two sites of Sb<sub>2</sub>S<sub>3</sub>, namely the pristine Sb (Sb<sub>P</sub>) site and the Sb<sub>AIU</sub> site, as the NO adsorption is the initial critical step to trigger the NORR.46 Upon absorbing NO on the Sb<sub>P</sub> site (Fig. 3a), \*NO exhibits a rather small N=O elongation (1.163 Å, 1.159 Å for original NO) with negligible  $Sb_p$ -to-\*NO electron transfer (-0.02 |e|), which means poor NO adsorption on the Sb<sub>P</sub> site. As a sharp comparison, \*NO on the Sb<sub>AIU</sub> site (Fig. 3b) presents dramatic N=O bond elongation (1.205 Å) and Sb<sub>AIU</sub>-to-\*NO electron transfer (-0.13 |e|), indicating largely improved NO adsorption on Sb<sub>AIU</sub>. Additionally, the charge density difference (Fig. 3c) clearly shows strong \*NO/Sb<sub>AIU</sub> electronic interactions, where both remarkable positive and negative charge aggregations can be seen on \*NO, proving that SbAIU enables powerful NO activation via a "donation-backdonation" mechanism.

To investigate the entire NORR process, we initially conducted online differential electrochemical mass spectrometry (DEMS) measurements to experimentally probe the reaction intermediates formed on Sb<sub>2</sub>S<sub>3</sub> during the NORR electrolysis. The online DEMS spectra (Fig. S15†) reveal the generation of distinct NH<sub>3</sub> (m/z = 17) and NH<sub>2</sub>OH (m/z = 33) signals.

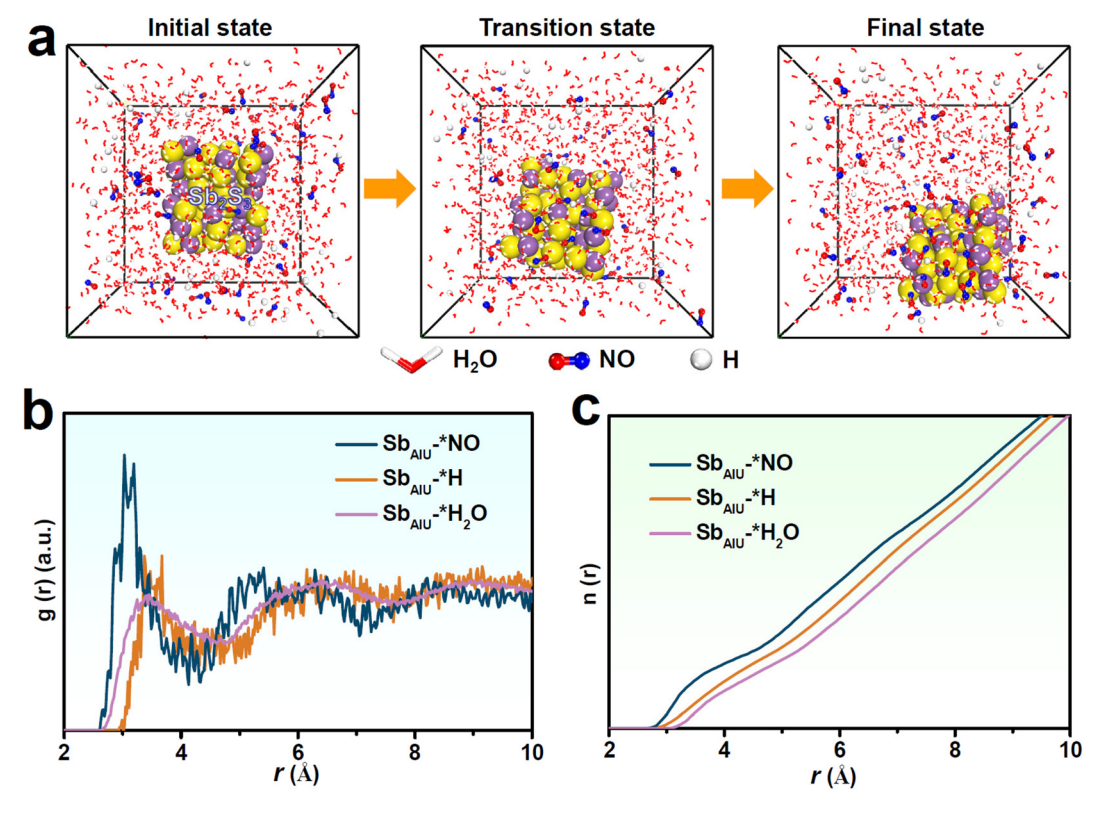


Fig. 4 (a) Initial, transition and final simulated states of the dynamic adsorption process of \*H<sub>2</sub>O, \*H and \*NO on Sb<sub>AIU</sub>, and the corresponding (b) RDF and (c) integrated RDF curves of the interactions between Sb<sub>AIU</sub> and \*NO, \*H and \*H<sub>2</sub>O.

Specifically, N (m/z = 14), which is the key intermediate involved in the NOH pathway, is absent in the NORR electrolysis, demonstrating that Sb<sub>2</sub>S<sub>3</sub> preferentially undergoes the NHO pathway to drive the NORR process,<sup>58</sup> as illustrated in Fig. 3d. As displayed in the free energy profiles of the energetic-preferred NHO pathway (Fig. 3e and Fig. S16†), the Sb<sub>p</sub> site exhibits a large energy barrier of 0.78 eV to drive the first protonation step of \*NO → \*NOH as the potential-determining step (PDS). In stark contrast, by virtue of powerful NO activation, the Sb<sub>AIU</sub> site presents a largely reduced barrier of 0.21 eV for the same \*NO → \*NOH, suggesting that the initial protonation step can be greatly boosted on the Sb<sub>AIU</sub> site. The PDS of Sb<sub>AIU</sub> is changed to \*NHOH  $\rightarrow$  \*NH<sub>2</sub>OH with only 0.36 eV uphill, corroborating the significantly enhanced NORR energetics over the SbAIU site that renders a high NORR activity of Sb<sub>2</sub>S<sub>3</sub>. We then investigated the catalytic behavior of the Sb<sub>AIU</sub> site towards the HER, which is the main competitive reaction for NORR.24 The calculated binding free energies (G) of various species (Fig. 3f) show that  $G_{*NO}$  (-0.44 eV) is much more negative than  $G_{*H,O}$  (1.05 eV) and  $G_{*H}$  (1.26 eV), demonstrating that the SbAIU site preferentially absorbs NO over H<sub>2</sub>O/H species to impede the competing HER.

Molecular dynamics (MD) simulations were conducted to further examine the competitive adsorption of NO and H<sub>2</sub>O/H on Sb<sub>AIU</sub>. After simulation, the snapshots (Fig. 4a) show prominent NO aggregation on SbAIU together with an enhanced SbAIIJ-\*NO interaction over SbAIIJ-\*H2O and SbAIIJ-\*H interactions, as displayed in the radial distribution function (RDF, Fig. 4b) curves and the corresponding integrated RDF curves (Fig. 4c), 58-62 proving a high tendency of Sb<sub>AIII</sub> for the adsorption and coverage of NO over H2O/H, which is greatly favorable for HER suppression to obtain a high NORR selectivity.

#### 3. Conclusion

In summary, Sb<sub>AIU</sub>-rich Sb<sub>2</sub>S<sub>3</sub> has been corroborated as a highperforming p-block metal catalyst for NORR. Theoretical computations reveal the critical role of SbAIU sites in promoting the activation and protonation of NO, while concurrently prohibiting the coverage of H<sub>2</sub>O/H species. This work not only highlights the critical design of atomically isolated and unsaturated sites to dramatically enhance the catalytic NORR activity and selectivity, but also demonstrates the promising prospects of p-block metal elements in the design of high-efficiency NORR electrocatalysts.

#### Conflicts of interest

There are no conflicts of interest to declare.

## Acknowledgements

This work was supported by the Longyuan Youth Innovative and Entrepreneurial Talents Project ([2021]17).

### References

- 1 J. Liang, Q. Liu, A. A. Alshehri and X. Sun, Recent advances in nanostructured heterogeneous catalysts for N-cycle electrocatalysis, Nano Res. Energy, 2022, 1, e9120010.
- 2 G. Wang, P. Shen, Y. Luo, X. Li, X. Li and K. Chu, A vacancy engineered MnO2-x electrocatalyst promotes electroreduction of nitrate to ammonia, Dalton Trans., 2022, 51, 9206-
- 3 X. Zhao, G. Hu, G. F. Chen, H. Zhang, S. Zhang and H. Wang, Comprehensive understanding of the thriving ambient electrochemical nitrogen reduction reaction, Adv. Mater., 2021, 33, 2007650.
- 4 Y. Luo, P. Shen, X. Li, Y. Guo and K. Chu, Sulfur-deficient Bi<sub>2</sub>S<sub>3-x</sub> synergistically coupling Ti<sub>3</sub>C<sub>2</sub>T<sub>x</sub>-MXene for boosting electrocatalytic N<sub>2</sub> reduction, Nano Res., 2022, 15, 3991-3999.
- 5 Y. Luo, O. Li, Y. Tian, Y. Liu and K. Chu, Amorphization engineered VSe2-x nanosheets with abundant Se-vacancies for enhanced N2 electroreduction, J. Mater. Chem. A, 2022, 10, 1742-1749.
- 6 K. Chu, Y. Luo, P. Shen, X. Li, Q. Li and Y. Guo, Unveiling the synergy of O-vacancy and heterostructure over MoO<sub>3-x</sub>/ MXene for N<sub>2</sub> electroreduction to NH<sub>3</sub>, Adv. Energy Mater., 2022, 12, 2103022.
- 7 Y. Cheng, X. Li, P. Shen, Y. Guo and K. Chu, MXene quantum dots/copper heterostructure for synergistically enhanced N2 electroreduction, Energy Environ. Mater., 2023, 6, e12268.
- 8 Z. Yan, M. Ji, J. Xia and H. Zhu, Recent advanced materials for electrochemical and photoelectrochemical synthesis of ammonia from dinitrogen: One step closer to a sustainable energy future, Adv. Energy Mater., 2020, 10, 1902020.
- 9 K. Tanifuji and Y. Ohki, Metal-sulfur compounds in N<sub>2</sub> reduction and nitrogenase-related chemistry, Chem. Rev., 2020, 120, 5194-5251.
- 10 G. Qing, R. Ghazfar, S. T. Jackowski, F. Habibzadeh, M. M. Ashtiani, C.-P. Chen, M. R. Smith and T. W. Hamann, Recent advances and challenges of electrocatalytic N2 reduction to ammonia, Chem. Rev., 2020, 120, 5437-5516.
- 11 B. H. Ko, B. Hasa, H. Shin, Y. Zhao and F. Jiao, Electrochemical reduction of gaseous nitrogen oxides on transition metals at ambient conditions, J. Am. Chem. Soc., 2022, 144, 1258-1266.
- 12 J. Long, S. Chen, Y. Zhang, C. Guo, X. Fu, D. Deng and J. Xiao, Direct electrochemical ammonia synthesis from nitric oxide, Angew. Chem., Int. Ed., 2020, 59, 9711-9718.
- 13 J. Choi, H.-L. Du, C. K. Nguyen, B. H. R. Suryanto, A. N. Simonov and D. R. MacFarlane, Electroreduction of nitrates, nitrites, and gaseous nitrogen oxides: A potential source of ammonia in dinitrogen reduction studies, ACS Energy Lett., 2020, 5, 2095-2097.
- 14 Y. Xiong, Y. Li, S. Wan, Y. Yu, S. Zhang and Q. Zhong, Ferrous-based electrolyte for simultaneous NO absorption

Research Article

- and electroreduction to NH<sub>3</sub> using Au/rGO electrode, *J. Hazard. Mater.*, 2022, **430**, 128451.
- 15 W. Zhang, X. Qin, T. Wei, Q. Liu, J. Luo and X. Liu, Single atomic cerium sites anchored on nitrogen-doped hollow carbon spheres for highly selective electroreduction of nitric oxide to ammonia, *J. Colloid Interface Sci.*, 2023, 638, 650–657.
- 16 J. Liang, P. Liu, Q. Li, T. Li, L. Yue, Y. Luo, Q. Liu, N. Li, B. Tang, A. A. Alshehri, I. Shakir, P. O. Agboola, C. Sun and X. Sun, Amorphous boron carbide on titanium dioxide nanobelt arrays for high-efficiency electrocatalytic NO reduction to NH<sub>3</sub>, *Angew. Chem.*, *Int. Ed.*, 2022, 61, e202202087.
- 17 Q. Wu, H. Wang, S. Shen, B. Huang, Y. Dai and Y. Ma, Efficient nitric oxide reduction to ammonia on a metal-free electrocatalyst, *J. Mater. Chem. A*, 2021, **9**, 5434–5441.
- 18 J. Long, C. Guo, X. Fu, H. Jing, G. Qin, H. Li and J. Xiao, Unveiling potential dependence in NO electroreduction to ammonia, J. Phys. Chem. Lett., 2021, 12, 6988–6995.
- 19 S. Cheon, W. J. Kim, D. Y. Kim, Y. Kwon and J.-I. Han, Electro-synthesis of ammonia from dilute nitric oxide on a gas diffusion electrode, ACS Energy Lett., 2022, 7, 958– 965.
- 20 Y. Xiao and C. Shen, Transition-metal borides (MBenes) as new high-efficiency catalysts for nitric oxide electroreduction to ammonia by a high-throughput approach, *Small*, 2021, 17, 2100776.
- 21 T. Wei, H. Bao, X. Wang, S. Zhang, Q. Liu, J. Luo and X. Liu, Ionic liquid-assisted electrocatalytic NO reduction to NH<sub>3</sub> by P-doped MoS<sub>2</sub>, *ChemCatChem*, 2023, 15, e202201411.
- 22 D. Qi, F. Lv, T. Wei, M. Jin, G. Meng, S. Zhang, Q. Liu, W. Liu, D. Ma, M. S. Hamdy, J. Luo and X. Liu, High-efficiency electrocatalytic NO reduction to NH<sub>3</sub> by nanoporous VN, *Nano Res. Energy*, 2022, 1, e9120022.
- 23 J. Liang, Q. Zhou, T. Mou, H. Chen, L. Yue, Y. Luo, Q. Liu, M. S. Hamdy, A. A. Alshehri, F. Gong and X. Sun, FeP nanorod array: A high-efficiency catalyst for electroreduction of NO to NH<sub>3</sub> under ambient conditions, *Nano Res.*, 2022, 15, 4008–4013.
- 24 K. Chen, G. Zhang, X. Li, X. Zhao and K. Chu, Electrochemical NO reduction to NH<sub>3</sub> on Cu single atom catalyst, *Nano Res.*, 2023, DOI: 10.1007/s12274-023-5384-9.
- 25 K. Chen, J. Wang, H. Zhang, D. Ma and K. Chu, Self-tandem electrocatalytic NO reduction to NH<sub>3</sub> on a W single-atom catalyst, *Nano Lett.*, 2023, 23, 1735–1742.
- 26 K. Chen, Y. Tian, Y. Li, Y.-P. Liu and K. Chu, Amorphous NiB<sub>2</sub> for electroreduction of NO to NH<sub>3</sub>, *J. Mater. Chem. A*, 2023, **11**, 7409–7414.
- 27 K. Chen, P. Shen, N. Zhang, D. Ma and K. Chu, Electrocatalytic NO reduction to NH<sub>3</sub> on Mo<sub>2</sub>C nanosheets, *Inorg. Chem.*, 2023, **62**, 653–658.
- 28 Y. Sun, Y. Wang, H. Li, W. Zhang, X.-M. Song, D.-M. Feng, X. Sun, B. Jia, H. Mao and T. Ma, Main group metal elements for ambient-condition electrochemical nitrogen reduction, *J. Energy Chem.*, 2021, **62**, 51–70.

- 29 L. Li, C. Tang, H. Jin, K. Davey and S.-Z. Qiao, Main-group elements boost electrochemical nitrogen fixation, *Chem*, 2021, 7, 3232–3255.
- 30 C. Lv, J. Liu, C. Lee, Q. Zhu, J. Xu, H. Pan, C. Xue and Q. Yan, Emerging p-block-element-based electrocatalysts for sustainable nitrogen conversion, *ACS Nano*, 2022, **16**, 15512–15527.
- 31 X. Li, G. Zhang, P. Shen, X. Zhao and K. Chu, A defect engineered p-block  $SnS_{2-x}$  catalyst for efficient electrocatalytic NO reduction to NH<sub>3</sub>, *Inorg. Chem. Front.*, 2023, **10**, 280–287.
- 32 K. Chen, Y. Zhang, J. Xiang, X. Zhao, X. Li and K. Chu, p-block antimony single-atom catalysts for nitric oxide electroreduction to ammonia, *ACS Energy Lett.*, 2023, **8**, 1281–1288.
- 33 K. Chen, G. Wang, Y. Guo, D. Ma and K. Chu, Iridium single-atom catalyst for highly efficient NO electroreduction to NH<sub>3</sub>, *Nano Res.*, 2023, DOI: 10.1007/s12274-023-5556-7.
- 34 K. Chen, N. Zhang, F. Wang, J. Kang and K. Chu, Maingroup indium single-atom catalysts for efficient electrocatalytic NO reduction to NH<sub>3</sub>, *J. Mater. Chem. A*, 2023, **11**, 6814–6819.
- 35 X. Liu, H. Jang, P. Li, J. Wang, Q. Qin, M. G. Kim, G. Li and J. Cho, Antimony-based composites loaded on phosphorus-doped carbon for boosting Faradaic efficiency of the electrochemical nitrogen reduction reaction, *Angew. Chem., Int. Ed.*, 2019, **58**, 13329–13334.
- 36 S. K. Kaiser, Z. Chen, D. Faust Akl, S. Mitchell and J. Pérez-Ramírez, Single-atom catalysts across the periodic table, *Chem. Rev.*, 2020, 120, 11703–11809.
- 37 C. Gao, J. Low, R. Long, T. Kong, J. Zhu and Y. Xiong, Heterogeneous single-atom photocatalysts: fundamentals and applications, *Chem. Rev.*, 2020, **120**, 12175–12216.
- 38 L. Zhang, M. Zhou, A. Wang and T. Zhang, Selective hydrogenation over supported metal catalysts: from nanoparticles to single atoms, *Chem. Rev.*, 2019, **120**, 683–733.
- 39 Q. Li, Y. Guo, Y. Tian, W. Liu and K. Chu, Activating VS<sub>2</sub> basal planes for enhanced NRR electrocatalysis: the synergistic role of S-vacancies and B dopants, *J. Mater. Chem. A*, 2020, **8**, 16195–16202.
- 40 K. Chu, J. Wang, Y. Liu, Q. Li and Y. Guo, Mo-doped SnS<sub>2</sub> with rich S-vacancies for highly efficient electrocatalytic N<sub>2</sub> reduction: the critical role of Mo-Sn-Sn trimer, *J. Mater. Chem. A*, 2020, 8, 7117–7124.
- 41 H. Du, H. Guo, K. Wang, X. Du, B. A. Beshiwork, S. Sun, Y. Luo, Q. Liu, T. Li and X. Sun, Durable electrocatalytic reduction of nitrate to ammonia over defective pseudobrookite Fe<sub>2</sub>TiO<sub>5</sub> nanofibers with abundant oxygen vacancies, *Angew. Chem., Int. Ed.*, 2023, **135**, e202215782.
- 42 A. Maiti and S. K. Srivastava, N, Ru codoped pellet drum bundle-like Sb<sub>2</sub>S<sub>3</sub>: An efficient hydrogen evolution reaction and hydrogen oxidation reaction electrocatalyst in alkaline medium, *ACS Appl. Mater. Interfaces*, 2020, **12**, 7057–7070.
- 43 X. Chen, X. Li, P. Wei, X. Ma, Q. Yu and L. Liu, Selective synthesis of Sb<sub>2</sub>S<sub>3</sub> nanostructures with different mor-

- phologies for high performance in dve-sensitized solar cells, Chin. J. Catal., 2020, 41, 435-441.
- 44 S. Yao, J. Cui, Y. Deng, W. G. Chong, J. Wu, M. Ihsan-Ul-Haq, Y.-W. Mai and J.-K. Kim, Ultrathin Sb<sub>2</sub>S<sub>3</sub> nanosheet anodes for exceptional pseudocapacitive contribution to multi-battery charge storage, Energy Storage Mater., 2019, 20, 36-45.
- 45 Y. S. Park, X. Jin, J. Tan, H. Lee, J. Yun, S. Ma, G. Jang, T. Kim, S. G. Shim and K. Kim, High-performance Sb<sub>2</sub>S<sub>3</sub> photoanode enabling iodide oxidation reaction for unbiased photoelectrochemical solar fuel production, Energy Environ. Sci., 2022, 15, 4725-4737.
- 46 K. Chen, J. Wang, J. Kang, X. Lu, X. Zhao and K. Chu, Atomically Fe-doped MoS2-x with Fe-Mo dual sites for efficient electrocatalytic NO reduction to NH3, Appl. Catal., B, 2023, 324, 122241.
- 47 L. Zhang, J. Zhang, A. Xu, Z. Lin, Z. Wang, W. Zhong, S. Shen and G. Wu, Charge redistribution of Co<sub>9</sub>S<sub>8</sub>/MoS<sub>2</sub> heterojunction microsphere enhances electrocatalytic hydrogen evolution, Biomimetics, 2023, 8, 104.
- 48 L. Zhang, Z. Wang, J. Zhang, Z. Lin, Q. Zhang, W. Zhong and G. Wu, High activity and stability in Ni<sub>2</sub>P/(Co,Ni)OOH heterointerface with a multiple-hierarchy structure for alkaline hydrogen evolution reaction, Nano Res., 2023, DOI: 10.1007/s12274-022-5322-2.
- 49 X. Wang, J. Zhang, Z. Wang, Z. Lin, S. Shen and W. Zhong, Fabricating Ru single atoms and clusters on CoP for boosted hydrogen evolution reaction, Chin. J. Struct. Chem., 2023, DOI: 10.1016/j.cjsc.2023.100035.
- 50 Y. Huang, Z. Hu, L.-a. Huang, Z. Wang, Z. Lin, S. Shen, W. Zhong and J. Pan, Phosphorus-modified cobalt singleatom catalysts loaded on crosslinked carbon nanosheets for efficient alkaline hydrogen evolution reaction, Nanoscale, 2023, 15, 3550-3559.
- 51 N. Zhang, G. Zhang, P. Shen, H. Zhang, D. Ma and K. Chu, Lewis acid Fe-V pairs promote nitrate electroreduction to ammonia, Adv. Funct. Mater., 2023, 33, 2211537.
- 52 G. Wang, P. Shen, K. Chen, Y.-L. Guo, X. Zhao and K. Chu, Rare-earth La-doped  $VS_{2-x}$  for electrochemical nitrate reduction to ammonia, Inorg. Chem. Front., 2023, 10, 2014-2021.

- 53 K. Chen, Z. Ma, X. Li, J. Kang, D. Ma and K. Chu, Singleatom Bi alloyed Pd metallene for nitrate electroreduction to ammonia, Adv. Funct. Mater., 2023, 33, 2209890.
- 54 W. Zhang, M. Jiang, S. Yang, Y. Hu, B. Mu, Z. Tie and Z. Jin, In situ grown  $CuO_x$  nanowire forest on copper foam: A 3D hierarchical and freestanding electrocatalyst with enhanced carbonaceous product selectivity in CO2 reduction, Nano Res. Energy, 2022, 1, e9120033.
- 55 N. Zhang, G. Zhang, Y. Tian, Y. Guo and K. Chu, Boron phosphide as an efficient metal-free catalyst for nitrate electroreduction to ammonia, Nano Res. Energy, 2023, 52, 4290-4295.
- 56 F. Guo, M. Zhang, S. Yi, X. Li, R. Xin, M. Yang, B. Liu, H. Chen, H. Li and Y. Liu, Metal-coordinated porous polydopamine nanospheres derived Fe<sub>3</sub>N-FeCo encapsulated N-doped carbon as a highly efficient electrocatalyst for oxygen reduction reaction, Nano Res. Energy, 2022, 1, e9120027.
- 57 Y. Cheng, P. Shen, X. Li, X. Li, K. Chu and Y. Guo, Synergistically enhanced peroxidase-like activity of Fe<sub>3</sub>O<sub>4</sub>/ Ti<sub>3</sub>C<sub>2</sub> MXene quantum dots and its application in colorimetric determination of Cr(v1), Sens. Actuators, B, 2023, 376, 132979.
- 58 X. Li, K. Chen, X. Lu, D. Ma and K. Chu, Atomically dispersed Co catalyst for electrocatalytic NO reduction to NH<sub>3</sub>, Chem. Eng. J., 2023, 454, 140333.
- 59 P. Shen, X. Li, Y. Luo, Y. Guo, X. Zhao and K. Chu, Highefficiency N2 electroreduction enabled by Se-vacancy-rich  $WSe_{2-x}$  in water-in-salt electrolytes, ACS Nano, 2022, 16, 7915-7925.
- 60 G. Zhang, X. Li, K. Chen, Y. Guo, D. Ma and K. Chu, Tandem electrocatalytic nitrate reduction to ammonia on MBenes, Angew. Chem., Int. Ed., 2023, 62, e202300054.
- 61 Y. Luo, K. Chen, G. Wang, G. Zhang, N. Zhang and K. Chu, Ce-doped MoS<sub>2-x</sub> nanoflower arrays for electrocatalytic nitrate reduction to ammonia, Inorg. Chem. Front., 2023, 10, 1543-1551.
- 62 X. Li, P. Shen, X. Li, D. Ma and K. Chu, Sub-nm RuO<sub>x</sub> clusters on Pd metallene for synergistically enhanced nitrate electroreduction to ammonia, ACS Nano, 2023, 17, 1081-1090.